Tailoring Optical Properties of Rare-Earth Doped Oxyfluoride Glass-Ceramics by Tuning Crystal Structure

Li, Zhencai; Hu, Jie; Du, Zijuan; Ge, Xuan; Jensen, Lars R.; Zhou, Dacheng; Yang, Yong; Smedskjaer, Morten M.; Qiu, Jianbei; Yue, Yuanzheng

Published in:
Advanced Optical Materials

DOI (link to publication from Publisher):
10.1002/adom.202401648

Publication date:
2024

Document Version
Publisher's PDF, also known as Version of record

RESEARCH ARTICLE

ADVANCED OPTICAL MATERIALS
www.advopticalmat.de

Tailoring Optical Properties of Rare-Earth Doped Oxyfluoride Glass-Ceramics by Tuning Crystal Structure

Zhencai Li, Jie Hu, Zijuan Du, Xuan Ge, Lars R. Jensen, Dacheng Zhou, Yong Yang, Morten M. Smedskjaer, Jianbei Qiu, and Yuanzheng Yue**

It is known that oxyfluoride glasses can be used as the host for fluoride crystals that feature promising optical properties. This work demonstrates that the optical properties of the Er^{3+}-Yb^{3+} co-doped oxyfluoride precursor glass-ceramic (PGC) can be tailored by changing crystal structure through chemical variation (LaF_3/BaF_2 = 0, 1/3; YF_3/LaF_3 ratios = 0, 2/7, 4/7, 6/7, 1) and heat treatment. The strong correlations between the crystallization behavior, microstructure, and optical properties are revealed. It is found that the precipitated crystals such as BaF_2, Ba_2LaF_7, $Ba_{2-x}La_{1-x}Y_xF_{7-2x}$ ($0 < x < 1$), and $BaYF_5$ are uniformly distributed in the glass matrices of PGC. Upon heat-treatment, the crystallinity of PGC increases, whereas the crystal type remains unchanged. Both the up-conversion luminescence and optical transmittance of the samples strongly depend on the substitution of one type of fluoride for another. Moreover, by taking advantage of the effect of crystal structure on the cross-relaxation propensity of Er^{3+} ions, it is feasible to tune the up-conversion luminescence color from green to light yellow. It is unveiled that the enhanced cross-relaxation arises from lattice shrinkage. This work provides guidance for optimizing the optical properties of rare-earth-doped oxyfluoride glass ceramics.

1. Introduction

Rare earth (RE) ions are well-known for their luminescent properties and, hence, have been utilized in displays and light-emitting diodes for decades.[1] Oxyfluoride glass-ceramics (GCs) are an ideal host material for RE ions as they provide a low-phonon-energy environment of fluoride crystals for RE ions, yet feature the chemical and mechanical stability of the oxide matrix.[2,3] Particularly, RE ions are preferentially incorporated into the fluoride nanocrystals embedded in the oxide glassy matrix. This makes these GC materials a promising medium for efficient visible and infrared emissions, enabling potential applications in various fields, including 3D displays,[4] light-emitting diodes,[5] solid-state lasers,[6] bioimaging,[7] and temperature-sensing.[8] However, to realize these promising applications, the up-conversion luminescence (UCL) of the transparent RE-doped oxyfluoride GCs needs to be further enhanced.

The factors affecting the UCL intensity include ambient temperature, energy level structure of RE ions, phonon energy of the fluoride crystals, and crystalline structure. Notably, the phonon energy of fluoride crystals can be tuned by varying the chemical composition of the precursor glass. Fluoride crystals with low phonon energy are desirable for extending the lifetime of excited states and thus enhancing the UCL. Therefore, scientists developed oxyfluoride GCs containing fluoride nanocrystals

Z. Li, X. Ge, M. M. Smedskjaer, Y. Yue
Department of Chemistry and Bioscience
Aalborg University
Aalborg DK-9220, Denmark
E-mail: yy@bio.aau.dk

Z. Li, D. Zhou, Y. Yang, J. Qiu
Faculty of Material Science and Engineering
Kunming University of Science and Technology
Kunming 650093, China
E-mail: qiu@kmust.edu.cn

The ORCID identification number(s) for the author(s) of this article can be found under https://doi.org/10.1002/adom.202401648

DOI: 10.1002/adom.202401648

J. Hu
Xiamen Research Center of Rare Earth Materials
Haixi Institutes
Chinese Academy of Sciences
Xiamen 361021, China

J. Hu
Fujian Institute of Research on the Structure of Matter
Chinese Academy of Sciences
Fuzhou 350002, China

Z. Du
State Key Laboratory of Silicate Materials for Architectures
Wuhan University of Technology
Wuhan 430070, China

L. R. Jensen
Department of Materials and Production
Aalborg University
Aalborg DK-9220, Denmark

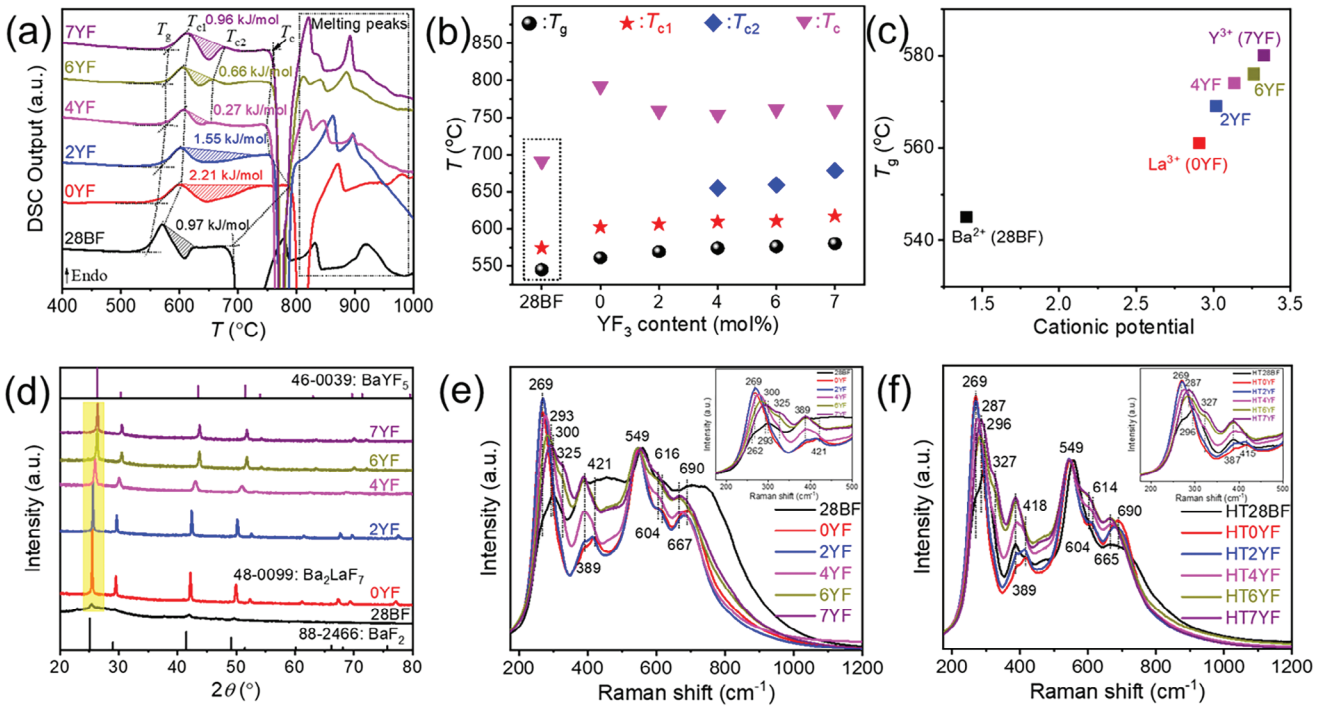

Figure 1. a) DSC upscan curves of PGC samples (Table 2). Note that the onset temperatures of both the glass transition, the first, second, and main crystallization peaks (T_g, T_{c1}, $T_{c2,}$ and T_c, respectively), and the melting regions are marked in Figure 1a; b) The varying tendency of T_g, T_{c1}, $T_{c2,}$ and T_c for PGC samples. c) The dependence of the glass transition to the cationic potentials of Ba^{2+} ions in 28BF, La^{3+} ions in 0YF, La^{3+} (Y^{3+}) ions in 2YF, 4YF, 6YF, and Y^{3+} ions in 7YF; d) XRD patterns of PGC samples, note: the shift of Bragg peak ≈25.5° of PGC samples are marked by highlight, the magnified XRD pattern is shown in Figure S2 (Supporting Information); e,f) Normalized Raman spectra of PGC samples (e) and heat-treated PGC (HTGC) samples (f), where the vibrational modes and the peak positions are indicated. All the Raman spectra are normalized by the intensity of the peak at ≈549 cm^{-1}.

with low phonon energy such as CaF_2 (484 cm^{-1}),[9] SrF_2 (397 cm^{-1}),[10] LaF_3 (350 cm^{-1}),[11] BaF_2 (346 cm^{-1}),[12] and YF_3 (300 cm^{-1}).[13] Recently, lanthanide ions doped oxyfluoride GCs containing BaF_2-based fluorite-type fluoride crystals such as $BaGdF_5$ (457 cm^{-1}),[14] $BaYbF_5$, and Ba_2LaF_7 (270 cm^{-1})[15] have been developed for hosting RE ions.

The traditional approach for preparing oxyfluoride GCs involves heat treatment (HT) of the precursor glass and is thus time- and energy-intensive. As an important advancement, a series of oxyfluoride GCs bearing BaF_2-based fluorite-type fluoride crystals were fabricated by melt-quenching without the HT process.[16] These melt-quenched GCs exhibit a stronger tendency to phase separate and higher UCL intensity compared to those containing the same type of fluoride crystals, which were produced by HT. It was proved that the melt-quenched GCs were the ideal hosts for RE ions to achieve high UCL intensity. However, it has been a challenge to control the type of fluoride crystals within the oxyfluoride GCs.[17,18] Thus, to address this challenge, it is necessary to further investigate the impact of chemical composition on both phase separation, crystallization behavior, and optical properties of oxyfluoride glasses. To do so, we performed the present study.

In this study, we prepared oxyfluoride GCs exhibiting strong UCL by partially replacing BaF_2 for LaF_3 as well as by fully substituting YF_3 for LaF_3 in the precursor composition $45SiO_2$-$15Al_2O_3$-$12Na_2O$-$28BaF_2$-$0.5ErF_3$-$1YbF_3$. We studied the impact of chemical composition on structural evolution and crystalline transformation by X-ray diffraction (XRD), Raman spectroscopy, scanning electron microscopy (SEM), and transmission electron microscopy (TEM) analyses. In addition, the temperature-induced phase transitions were investigated by differential scanning calorimetry (DSC). Finally, we revealed the dependence of optical properties, including optical transmittance, UCL, and cross-relaxation (CR) of the Er^{3+} ions, on glass structure, crystal structure, and thermal treatment.

2. Results and Discussion

2.1. Calorimetric and Structural Analyses

Figure 1a shows the DSC upscan curves of precursor glass-ceramic (PGC) samples (Table 2). Both the onset glass transition temperature (T_g) and the onset temperatures of the first, second, and main crystallization peaks (T_{c1}, $T_{c2,}$ and T_c, respectively) are determined as described elsewhere.[19] The melting peaks are marked by the black dotted box. The obtained values of the characteristic temperatures are shown in Table S1 (Supporting Information), in which T_g and T_{c1} increase with the substitution of Ba^{2+} with La^{3+} and then La^{3+} with Y^{3+} (Figure 1b). This implies an increase in both the fraction of $[Si(Al)O_4]$ tetrahedral units and the glass network connectivity in the glass matrix.[16] In addition to the first crystallization behavior, a second crystallization peak in the DSC curves appears for 4YF, 6YF, and 7YF, with T_{c2} increasing with the YF_3 content. The T_c for the main crystallization

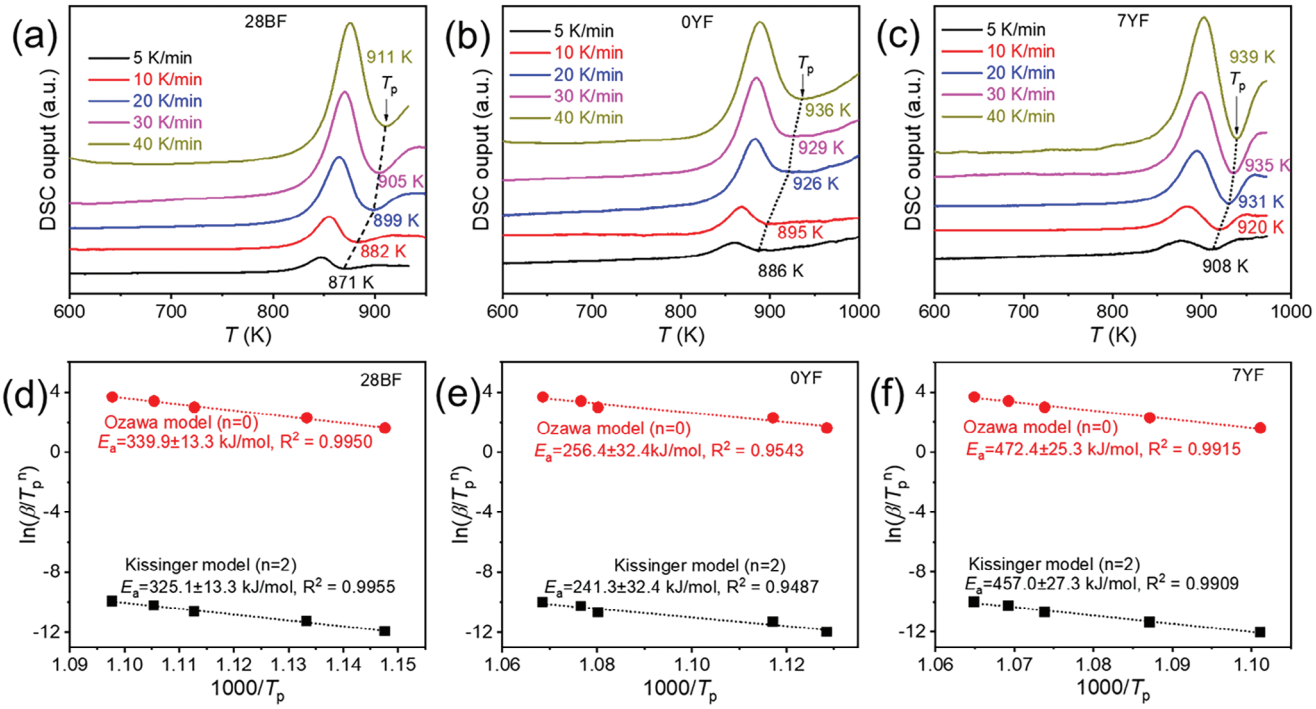

Figure 2. a–c) DSC curves of 28BF, 0YF, and 7YF were obtained at the heating rate of 5, 10, 20, 30, and 40 K/min, respectively. Note that the crystallization peak temperatures (T_p) are marked in these curves; d–f) Plots of $\ln(\beta/T_p^n)$ to $1000/T_p$ of 28BF, 0YF, and 7YF, where n = 0 corresponds to the Ozawa model, n = 2 refers to the Kissinger model. The crystallization activation energy (*Ea*) of 28BF, 0YF, and 7YF was estimated by fitting with the two models.

peak first increases sharply and then slightly varies with composition.

To understand the origin of the composition dependence of the glass transition of the studied samples, T_g is plotted in Figure 1c against cationic potential. The cationic potential $\Phi = Z/r$ is the crucial factor in influencing the degree of phase separation. The higher the Φ value is, the greater the possibility of the glass phase separation. Specifically, modifiers with higher cationic potential can more easily attract bridging oxygens in the tetrahedral network structure (aluminosilicate-rich phase). Figure 1c shows that the cationic potential follows the trend of $\Phi(Ba^{2+})$ in 28BF $< \Phi(La^{3+})$ in 0YF $< \Phi(Y^{3+})$ in 7YF. In addition, the binding energy of Ba—O(F) is lower than that of both La—O(F) and Y—O(F). The smaller cationic potential may make the aluminosilicate-rich phase and fluoride-rich phase more difficult to separate. Thus, Ba^{2+} ions have a higher probability of being evenly distributed in the glass phase, thereby dissociating the structural network, and lowering T_g. Compared with Ba^{2+} ions, La^{3+} and Y^{3+} ions could be mainly located in the fluoride-rich phase, leading to a slight increase in T_g.

To investigate the first crystallization event in the PGC samples (manifested by the first exothermic peak in Figure 1a), the crystallization enthalpy (ΔH) of the studied samples was calculated by determining the area of the first exothermic peak. Figure 1a shows that ΔH first increases sharply and then decreases and finally increases again with composition. This indicates that the crystallization behavior is initially promoted and then varies with increasing the YF_3 content. The kinetics of the first crystallization event in 28BF, 0YF, and 7YF are also studied using a non-isothermal method. It is seen that the T_p (the first crystallization peak temperature) varies with the heating rate. The T_p values at the heating rates of 5, 10, 20, 30, and 40 K per min for 28BF, 0YF, and 7YF are shown in **Figure** 2a–c. The heating rate dependence of T_p is used for calculating the crystallization activation energy (E_a) via the Ozawa model ($n = 0$) and the Kissinger model ($n = 2$):[20]

$$\ln\left(\frac{\beta}{T_p^{\,n}}\right) = -\frac{E_a}{RT_p} + const \quad (1)$$

where β is the heating rate, and R is the universal gas constant 8.314 J/(mol·K). The E_a values of 28BF are obtained from both the Ozawa and the Kissinger models to be 339.9 and 325.1 kJ mol^{-1}, respectively (Figure 2d). In contrast, the two E_a values of 0YF are 256.4 and 241 kJ mol^{-1} (Figure 2e), while those of 7YF are 472.4 and 457 kJ mol^{-1} (Figure 2f), respectively. Apparently, the two models yield comparable E_a values for each sample. E_a is related to a certain energy barrier. The higher the E_a is, the greater the energy barrier for the transformation of the glass phase into the crystalline phase of fluorides, i.e., the weaker the crystallization tendency is. Thus, 0YF exhibits the strongest crystallization tendency, whereas 7YF has the weakest tendency.

As shown in Figure S1a,b and Table S1 (Suppporting Information), HT leads to an increase in both T_g and T_{c1}. This effect is attributed to the increase in the number of connected [SiO_4] and [AlO_4] tetrahedral units in the glass matrix because of the precipitation of fluoride crystals (Figure 1d). Moreover, the ΔH of the heat-treated sample is smaller compared to the original sample.

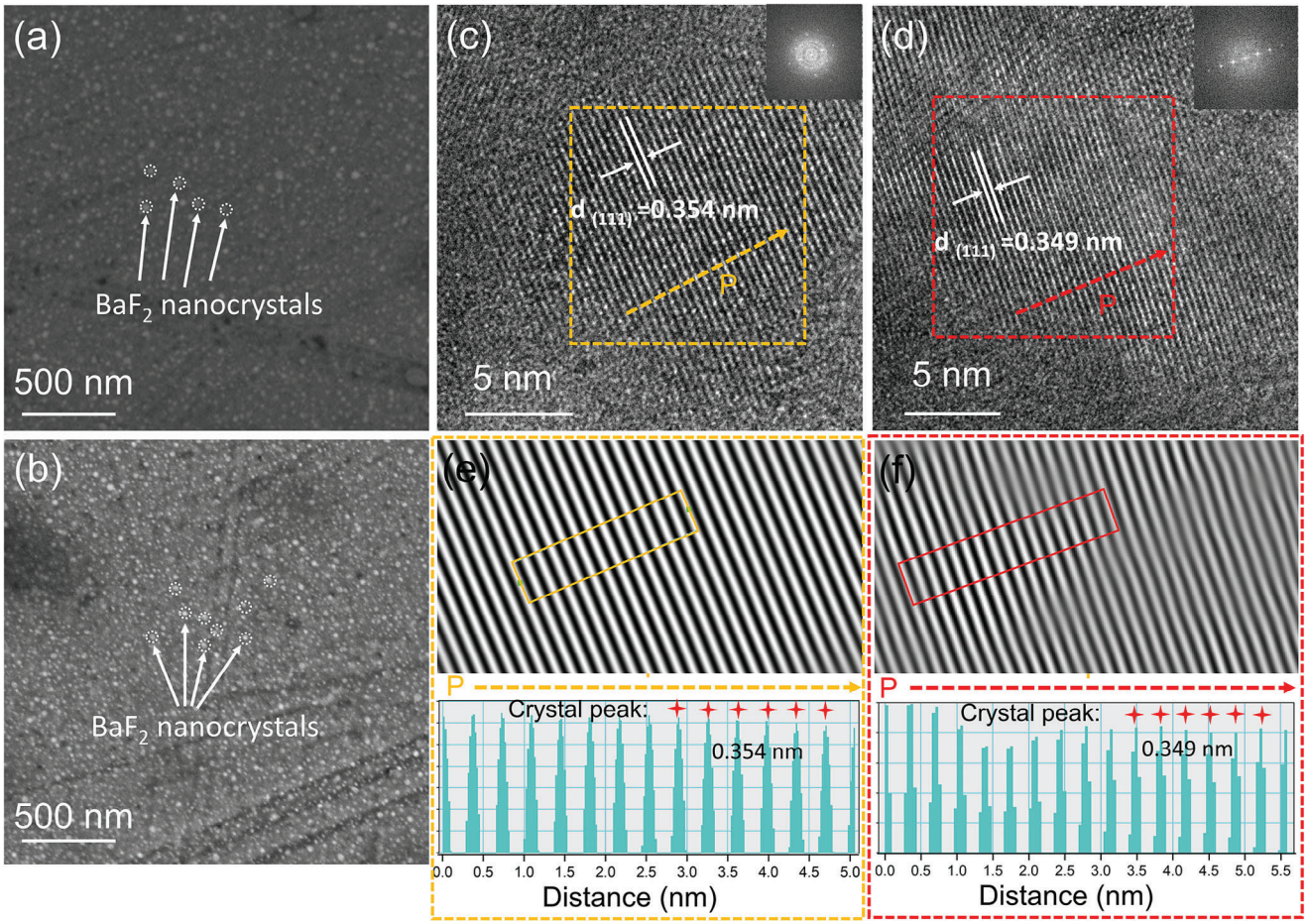

Figure 3. SEM images of 28BF a) and HT28BF b); HRTEM images of 28BF c) and HT28BF d), inset is the SAED pattern of the area marked by the red dashed box; e,f) inverse fast Fourier transform (IFFT) images of lattice fringes of the BaF_2 crystals as shown in (c) and (d), respectively. g,h) Intensity profiles of FFT were recorded by scanning along the directions of the orange and red arrows of the BaF_2 crystals as shown in (c) and (d), respectively.

This indicates that a certain number of crystals have already been precipitated in the samples during HT.

Figure 1d shows the XRD patterns of the PGC samples. It is seen that 28BF exhibits a broad hump with four weak Braggs peaks related to BaF_2, indicating that the amorphous phase is dominant. This suggests that a small amount of BaF_2 crystals have already formed in the glass matrix during melt-quenching.

Table 1. The absolute internal UPLQY of 28BF, 0YF, 4YF, 7YF, HT28BF, HT0YF, HT4YF, and HT7YF.

Samples	UPLQY (%)
28BF	0.00824
0YF	0.01879
4YF	0.00527
7YF	0.00376
HT28BF	0.03515
HT0YF	0.0617
HT4YF	0.00861
HT7YF	0.00505

In contrast, the rest samples show four sharp diffraction peaks, suggesting the predominance of the crystalline phase. A partial substitution of LaF_3 for BaF_2 leads to the appearance of cubic Ba_2LaF_7 crystals as shown in the XRD pattern of 0YF.[21] The peaks of the Ba_2LaF_7 crystal are located at larger angles compared to BaF_2 crystal (Figure S2, Supporting Information), suggesting the replacement of Ba^{2+} with La^{3+} ions in the crystal lattice.[22] It is also observed in Figure 1d that the shift of the XRD peaks toward larger angles by gradually replacing LaF_3 with YF_3. This observation implies the gradual formation of the solid solution of $Ba_{2-x}La_{1-x}Y_xF_{7-2x}$ within 2YF, 4YF, and 6YF, whereas only cubic $BaYF_5$ is present in 7YF.[8,23] This phenomenon is attributed to the substitution of large La^{3+} ions (1.06 Å) for small Y^{3+} ions (0.9 Å) in the crystal lattice.

Figure 1e,f shows the Raman spectra of both the PGC samples and the heated-treated PGC samples (named HTGC samples, shown in Table 2), the intensities of which are normalized by that of the peak at ≈549 cm^{-1}. The magnified Raman spectrum of 28BF (inset in Figure 1e) displays a weak peak at 262 cm^{-1} and a strong peak at 300 cm^{-1}. These two peaks become more pronounced in the Raman spectrum of HT28BF (Figure S3b,c, Supporting Information). The two peaks are attributed to the

vibrational mode of the Ba—F bond in BaF_2.[24] The Raman peak at 269 cm^{-1} in 0YF is ascribed to the strong vibration of Ba—F and La—F bonds in Ba_2LaF_7.[25] It is observed in Figure 1e that the Raman peak shifts from 269 to 293 cm^{-1}, while the intensity ratio between the Raman peak in the range from 269 to 293 cm^{-1} and that at 549 cm^{-1} slightly increases and then decreases with increasing the YF_3 content. This indicates that the La—F bond is gradually substituted by Y—F bonds. Additionally, a weak Raman peak gradually emerges at ≈325 cm^{-1} upon substituting YF_3 for LaF_3. Based on the above analyses, it is inferred that the Raman peaks at 293 and 325 cm^{-1} could be ascribed to the vibrations of the Ba-F and Y-F bonds in $BaYF_5$, respectively.

The Raman peaks at 389 and 421 cm^{-1} are associated with a symmetric ring-breathing mode (≥five fold ring structure), which involves oxygen motion. Moreover, the Raman peak at 389 cm^{-1} is enhanced by substituting YF_3 for LaF_3 while the peak at 421 cm^{-1} becomes weaker and then disappears.[16] The shift could be caused first by the substitution of Ba^{2+} with La^{3+} and then La^{3+} with Y^{3+} in bonds of Ba—NBO—Si(Al), La—NBO—Si(Al), and Y—NBO—Si(Al). The Raman peak moves from 690 to 667 cm^{-1} by replacing Ba^{2+} with La^{3+} and then LaF_3 with YF_3, while the peak shifts from 616 to 604 cm^{-1}. The mid-frequency bands at 549–690 cm^{-1} are associated with the Si—O—Si (Al) bending mode in the glass matrix. The peaks at 549 and 604 cm^{-1} are attributed to the vibrational modes of four- and three-membered rings, respectively.[25,26] The normalized Raman spectra of HTGC samples (Figure 1f) exhibit higher intensity than those in Figure 1e, indicating that both the network connectivity and the crystallinity increase upon HT. In summary, these Raman spectra provide insights into the structure changes both in the glass matrix and in crystals upon replacing BaF_2 for LaF_3 and then YF_3 for LaF_3.

2.2. Microstructure and Morphology

SEM and TEM measurements are conducted to investigate the microstructure of both the 28BF and HT28BF samples and the precipitated nanocrystals. **Figure 3a** shows an SEM image of 28BF, where spherical nanocrystals with an approximate diameter of 10 nm are observed in the glass phase. The BaF_2 nanocrystals are identified by both the high-resolution TEM (HRTEM) images (Figure 3c) and the corresponding fast Fourier transform patterns (inset of Figure 3c). The (111) crystalline plane of BaF_2 with the corresponding *d*-spacing values of 0.354 nm is determined from the lattice fringes (Figure 3e), which is marked by the yellow dashed arrow P (Figure 3c). Interestingly, as observed in the SEM images of HT28BF (Figure 3b), the existing BaF_2 nanocrystals do not grow but remain ≈10 nm, while new BaF_2 nanocrystals precipitate from glass matrix upon HT. However, the nanocrystals are identified as BaF_2 by comparing the (111) interplanar spacing (0.349 nm, Figure 3d) with the standard one. Here, the spacing is determined along the red dashed arrow P (Figure 3f). The crystal size remains unchanged since highly viscous layers (i.e., diffusion barrier) form at the interface between crystal and glass matrix during heating up to T_{c1} according to a previous study.[27] In turn, this ensures the optical transparency of HT28BF. The microstructures of 0YF, HT0YF, 7YF, and HT7YF were characterized in refs.[8,16] Furthermore, phase separation intensely occurs in 0YF and 7YF during melt-quenching, whereas Ba_2LaF_7 and $BaYF_5$ crystals grow in these samples during HT.

2.3. Optical Properties

Figure 4a,b shows the UCL spectra of PGC and HTGC samples in the wavelength range from 500 to 700 nm. Three sharp peaks of UCL are assigned to the $^2H_{11/2}\rightarrow{}^4I_{15/2}$ (523 nm), $^4S_{3/2}\rightarrow{}^4I_{15/2}$ (541 nm), and $^4F_{9/2}\rightarrow{}^4I_{15/2}$ (653 nm) transitions of Er^{3+} ions. As shown in Figure 4a, the UCL intensity first increases with substituting LaF_3 for BaF_2. However, as increasing the YF_3 content, the UCL intensity first increases and then decreases. The UCL intensity at 541 nm of 4YF is 32 times higher than that of 28BF. In contrast, the UCL intensity at 653 nm of 4YF is 128 times higher than that of 28BF (see the inset of Figure 4a). The ratio (*R*) between the UCL intensity of the peak at 653 nm and that at 541 nm for 4YF is higher than that for 28BF. To observe the *R* variation by substituting Ba^{2+} for La^{3+} and then La^{3+} for Y^{3+}, the UCL spectra of the PGC samples are normalized by the peak intensity of 541 nm (Figure 4c). The *R*-increasing trend with the above-mentioned substitution indicates an enhancement of the CR between the energy levels of Er^{3+} ions.[28] In addition, the variation in the UCL intensity for the HTGC series in Figure 4b follows almost the same trend as that for the PGC series. This trend also applies to the variation of *R* upon HT (Figure 4d). It is seen in Figure S4a (Supporting Information) that HT results in an *R* increase except for HT4YF, indicating an enhancement of CR.

To understand the UCL enhancement of Er^{3+} ions in the studied samples, the excitation power-dependent UCL is calculated. As is known, the UCL intensity (I_{UCL}) is proportional to the infrared excitation pumping power (I_{IR}): $I_{UCL}\propto(P_{IR})^n$, where *n* is the number of photons required to transfer from the ground state to the UCL states.[29] The *n* value is the slope of the linear relation of the $\log(I_{UCL})$ versus the $\log(P_{IR})$ plot. The logarithmic plots of pumping power-dependent UCL are presented in Figure S5a–d (Supporting Information), where the slopes of the fitted lines are ≈2 at both 541 and 653 nm. This indicates that the two-photon process is involved in the green and red UCL.

To further investigate the relation between the variation in UCL intensity and the corresponding UCL mechanism, the probability of energy transfer between Er^{3+} and Yb^{3+} ions is evaluated by the absolute internal up-conversion photoluminescence quantum yield (UPLQY in %). As shown in **Table 1**, despite its relatively smaller UPLQY value than that of the existing GC samples,[30] the absolute internal UPLQY of PGC samples first increases from 0.0082% to 0.0188% and then decreases to 0.0038% with a compositional change. This variation trend is almost similar to that for the UCL intensities, but the UPLQY of 28BF is higher than those of 4YF and 7YF. Moreover, the absolute internal UPLQY of PGC samples increases upon HT. The UPLQY of HT28BF is ≈4.3 times higher than that of 28BF. In contrast, the UPLQY of 0YF increases by 3.3 times upon HT, while that of 4YF and 7YF increases slightly. This indicates that Er^{3+} ions enter low phonon energy environment of fluoride crystals to decrease the possibility of non-radiative transition of Er^{3+} ions, thereby enhancing the UCL. To further understand the low

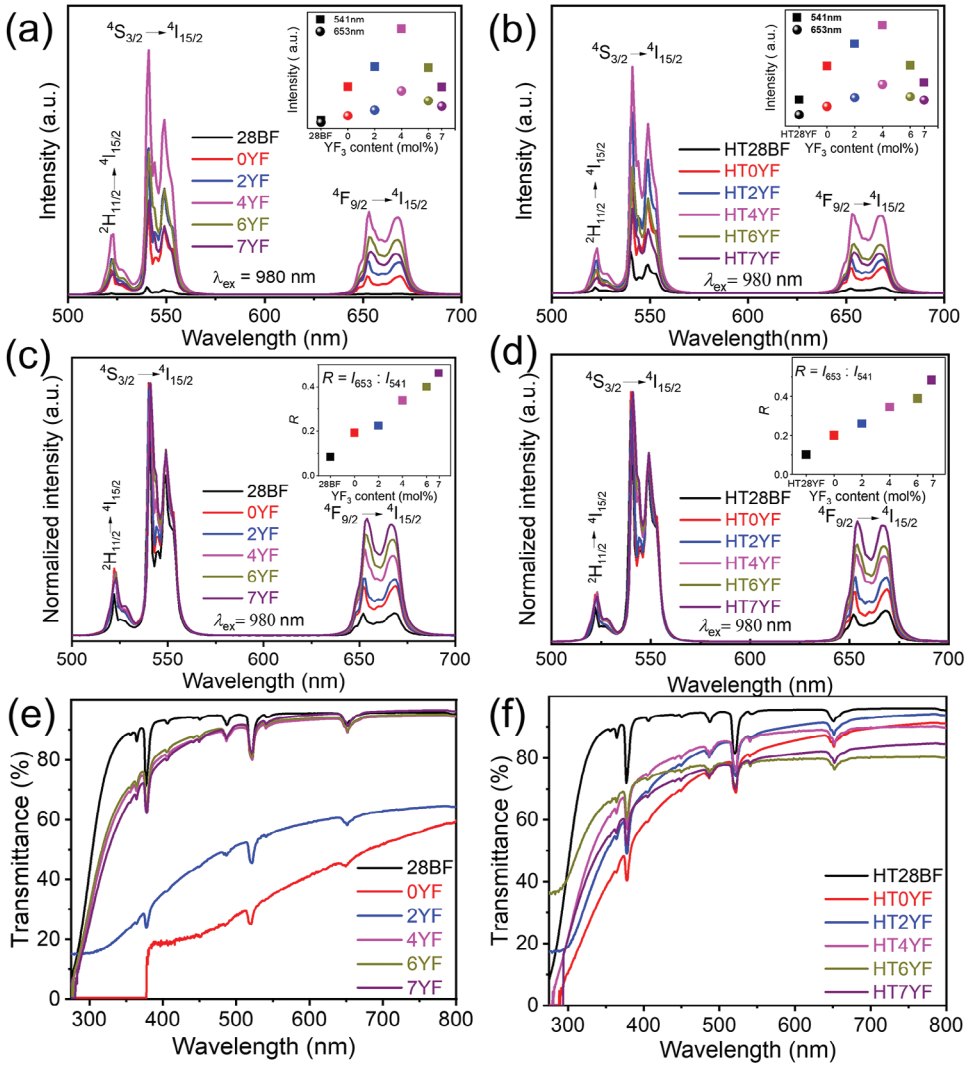

Figure 4. The UCL spectra of PGC a) and HTGC b) samples under the 980 nm excitation; The normalized UCL spectra of PGC c) and HTGC d) samples under the 980 nm excitation; The optical transmittance of PGC e) and HTGC f) samples.

phonon energy environment surrounding Er^{3+} ions, the local symmetry of Er^{3+} ions is determined using Eu^{3+} as probe ions.[31] The results show that the local symmetry of Er^{3+} ions of HT4YF is the lowest (0.51) (Figure S6a,b, Supporting Information) among the samples, and hence, the phonon energy of the environment surrounding Er^{3+} ions is the lowest, resulting in the strongest UCL.[31]

Figure 4c,d shows the optical transmittance (%) spectra in the wavelength range of 275 to 800 nm for the PGC and HTGC samples. The optical transmittance spectra are obtained from the absorption spectra (Figure S4c,d, Supporting Information). Figure 3c shows that the optical transmittance of 28BF first decreases with the substitution of LaF_3 for BaF_2 then increases up to ≈90%, and remains unchanged with the replacement of LaF_3 by YF_3. The decrease in optical transmittance of 28BF with the substitution of Ba^{2+} for La^{3+} can be clarified as follows. The crystallinity of 28BF is rather low compared to other samples, while the size of BaF_2 nanocrystals is ≈10 nm. This suggests that light scattering is negligible and thus the transparency is higher according to the Rayleigh–Gans theory.[32] However, compared to other samples, the Ba_2LaF_7 crystals in phase-separated 0YF are bigger, and hence the difference in refractive index between Ba_2LaF_7 crystal and glass matrix is larger.[16] This is why 0YF exhibits strong light scattering and hence a high degree of translucency. The size and crystallinity for other PGC samples become smaller with the substitution of YF_3 for LaF_3. This is confirmed by the Raman and XRD results. Moreover, the refractive index of the samples might decrease with the density of the samples (Figure S4b, Supporting Information) since the refractive index is proportional to the density of the samples.[33,34] Thus, the difference in refractive index between crystal and glass matrix might decrease upon HT, indicating an increase in the optical transmittance. The optical transmittance of HT28BF (Figure 3f) is similar to that of 28BF, suggesting that the formation of small spherical BaF_2 crystals does not cause a detectable change in the light scattering. However, the optical transmittance of HT4YF, HT6YF, and HT7YF is lower than that of their precursor samples since HT leads to crystal formation.

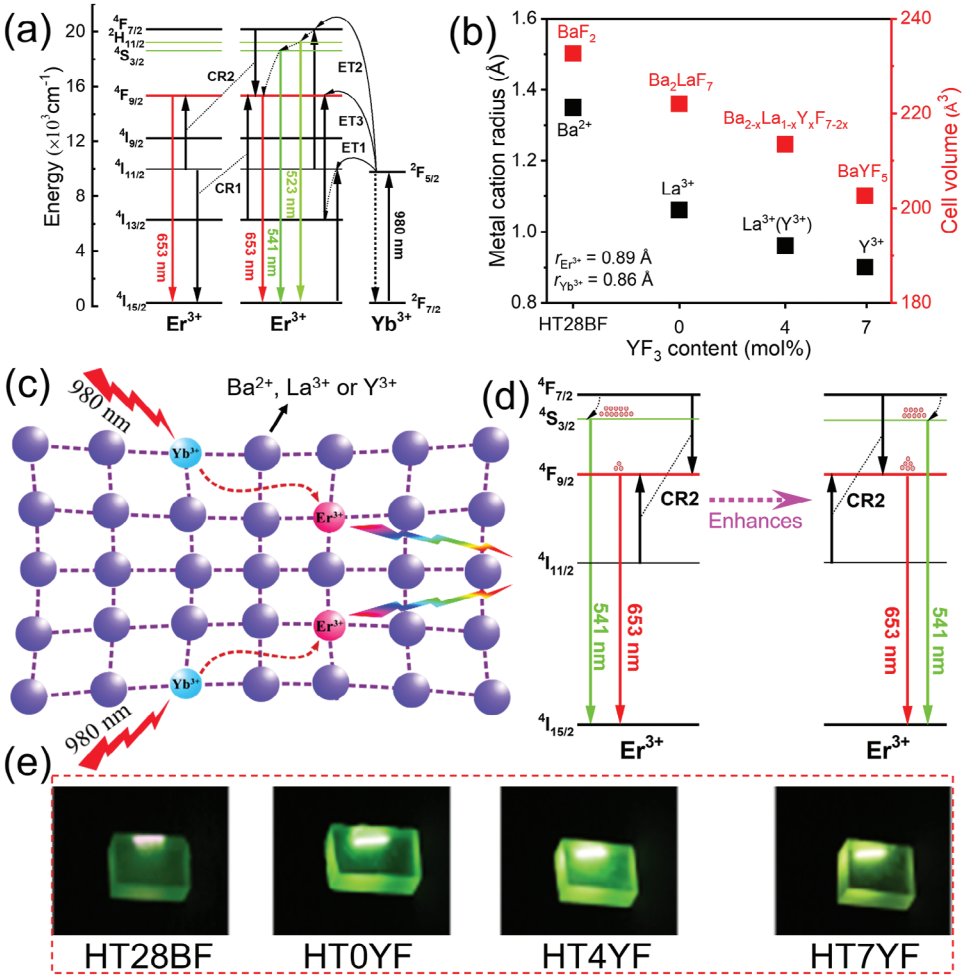

Figure 5. a) The possible mechanism of UCL and energy transfer processes of Er^{3+}-Yb^{3+} co-doped samples under the 980 nm diode laser excitation. b) The variation of metal cation radius and unit cell volume in the crystals of 28BF, 0YF, 4YF, and HT7YF, respectively. c) The schematic diagram of the lattice shrinkage in the BaF_2, Ba_2LaF_7, $Ba_{2-x}La_{1-x}Y_xF_{7-2x}$, and $BaYF_5$ crystals of HT28BF, HT0YF, HT4YF, and HT7YF, respectively. Noting: Er^{3+} and Yb^{3+} entered lattice by the substitution to Ba^{2+}, La^{3+}, and Y^{3+} ions, emitting UCL of HT28BF, HT0YF, HT4YF, and HT7YF shown in the red dashed box (c). e) The schematic diagram for the enhanced CR2 process causing an increase in the population of photonics at the $^4F_{7/2}$ level.

To investigate the CR process between the energy level of Er^{3+} ions in the studied samples, the energy level scheme of the Yb^{3+} and Er^{3+} ions under laser excitation of 980 nm was plotted in **Figure 5a**. The energy transfer between Yb^{3+} and Er^{3+} ions has been described in a previous study.[15] The enhancement of red UCL of Er^{3+} ions could be attributed to an increase in the ET3, CR1, and CR2 processes by substituting Ba^{2+} for La^{3+} and then La^{3+} for Y^{3+}. However, the probability of the CR1 and ET3 processes is low because the number of Er^{3+} ions at the energy level of $^4I_{13/2}$ is small.[35] In other words, it is difficult for Er^{3+} ions at the energy level of $^4I_{15/2}$ to transition back to the energy level of $^4I_{13/2}$ via non-radiative transition. This indicates that Er^{3+} ions at the energy level of $^4I_{13/2}$ absorb neither the energy from Yb^{3+} ions at the energy level of $^2F_{5/2}$ (ET3), nor the energy via the CR1 process for Er^{3+} ions to be excited from the $^4I_{13/2}$ to $^4F_{9/2}$ energy level. Therefore, the CR2 process is the primary mechanism causing the enhancement of red UCL.

To further study the origin of the enhancement of the CR2 process between energy levels of Er^{3+} ions by substituting Ba^{2+} for La^{3+} and then La^{3+} for Y^{3+}, the crystalline structure in the studied samples was characterized, thereby proposing a CR mechanism. It is seen in Figure 5b that the metal cation radius decreases from Ba to Y, leading to a decrease in interplanar spacing (*d*) and a shift of the XRD peak to larger angles (Figure 1d, Figure S2, Supporting Information). This indicates a lattice shrinkage of the unit cell volume (Figure 4b).[31] It is known that Er^{3+} or Yb^{3+} ions preferentially enter the lattice site of BaF_2, Ba_2LaF_7, $Ba_{2-x}La_{1-x}Y_xF_{7-2x}$, and $BaYF_5$ crystals by substituting Ba^{2+}, La^{3+}, La^{3+}(Y^{3+}) and Y^{3+} ions, respectively. To visualize the incorporation of Er^{3+} and Yb^{3+} ions into crystals, a schematic diagram is drawn in Figure 5c concerning the lattice shrinkage and incorporation of Er^{3+} and Yb^{3+} ions into BaF_2, Ba_2LaF_7, $Ba_{2-x}La_{1-x}Y_xF_{7-2x}$, and $BaYF_5$ crystals in HT28BF, HT0YF, HT4YF, and HT7YF, respectively. Although Ba^{2+} ions occupy the 4a Wyckoff positions in the BaF_2 crystals of HT28BF,[31] the possibility of the substitution of Er^{3+} (0.89 Å) for Ba^{2+} ions (1.35 Å) is low due to both the imbalance of cation valence states and the difference in ionic radius. Therefore, most Er^{3+} ions are likely located in the glass matrix rather than in the

Table 2. The chemical compositions of both the PGC and the HTGC samples.

Chemical composition	PGC	HTGC
$45SiO_2$-$15Al_2O_3$-$12Na_2O$-$28BaF_2$-$0.5ErF_3$-$1.0YbF_3$	28BF	HT28BF
$45SiO_2$-$15Al_2O_3$-$12Na_2O$-$21BaF_2$-$7LaF_3$-$0.5ErF_3$-$1.0YbF_3$	0YF	HT0YF
$45SiO_2$-$15Al_2O_3$-$12Na_2O$-$21BaF_2$-$2YF_3$-$5LaF_3$-$0.5ErF_3$-$1.0YbF_3$	2YF	HT2YF
$45SiO_2$-$15Al_2O_3$-$12Na_2O$-$21BaF_2$-$4YF_3$-$3LaF_3$-$0.5ErF_3$-$1.0YbF_3$	4YF	HT4YF
$45SiO_2$-$15Al_2O_3$-$12Na_2O$-$21BaF_2$-$6YF_3$-$1LaF_3$-$0.5ErF_3$-$1.0YbF_3$	6YF	HT6YF
$45SiO_2$-$15Al_2O_3$-$12Na_2O$-$21BaF_2$-$7YF_3$-$0.5ErF_3$-$1.0YbF_3$	7YF	HT7YF

BaF_2 crystals, leading to the weak UCL. However, for the Ba_2LaF_7 crystals in HT0YF, La^{3+} ions, which have a smaller ionic radius than Ba^{2+} ions, are probably replaced by Er^{3+} ions to occupy the same 4a Wyckoff positions as La^{3+} ions. By substituting Y^{3+} ions, Er^{3+} ions can be easily incorporated into $BaYF_5$ crystals because Er^{3+} ions have a similar radius as Y^{3+} ions. Therefore, the distance between Er^{3+} ions decreases with both the contraction of the unit cell volume of the crystals and the increase in the concentration of Er^{3+} ions in the crystals. This causes the near-resonant CR2 ($^4I_{11/2}$ (Er^{3+}) + $^2F_{7/2}$ (Er^{3+}) → $^4F_{9/2}$ (Er^{3+}) + $^4F_{9/2}$ (Er^{3+})) to be enhanced owing to the interaction between $^4F_{7/2}$ and $^4I_{11/2}$ levels of Er^{3+} ions (Figure 5d), leading to an increase in the population of photonics at the $^4F_{9/2}$ level and thus emitting intense red UCL. Thus, the UCL color of HT28BF, HT0YF, HT4YF, and HT7YF under the 980 nm laser excitation changes from green to light yellow (Figure 5e), coinciding with the observation in the CIE diagram (Figure S7, Supporting Information). In addition to the color change, the variation trend of UCL brightness is consistent with that of the UCL intensity. Here it should be mentioned that the change in both color and UCL intensity could have a strong effect on the potential LED performance of the studied materials according to the previous studies.[36,37]

3. Conclusion

A facile strategy of changing the initial composition of $45SiO_2$-$15Al_2O_3$-$12Na_2O$-$28BaF_2$-$0.5ErF_3$-$1.0YbF_3$ was established to prepare a series of glass ceramics via melt-quenching. The effect of substituting Ba^{2+} for La^{3+} and then La^{3+} for Y^{3+} in the chemical composition on the crystallization behavior, structural evolution, and optical properties of the studied samples was studied by performing DSC, XRD, Raman spectroscopy, SEM, and TEM characterizations and optical analyses. The results showed that the crystalline phase transforms from BaF_2 to Ba_2LaF_7, $Ba_{2-x}La_{1-x}Y_xF_{7-2x}$, and finally to $BaYF_5$ by substituting Ba^{2+} for La^{3+} and then La^{3+} for Y^{3+} in the precursor glass-ceramic (PGC) samples. Notably, the up-conversion luminescence (UCL) of the PGC samples was first significantly enhanced and then slightly weakened with the institution of Ba^{2+} for La^{3+} and then La^{3+} for Y^{3+}, while the optical transmittance exhibited the opposite scenario.

Moreover, the above-mentioned substitution in the PGC samples induced the cross-relaxation (CR) between the energy levels of Er^{3+} ions, which is attributed to the shrinkage of the lattice structure. The mechanism for the shrinkage of the lattice structure influences on CR was proposed. Additionally, heat-treatment can enhance not only the optical transmittance but also the UCL of the studied glass-ceramic samples. This study guided tailoring optical properties of rare-earth doped oxyfluoride glass-ceramics by tuning fluoride structure for various applications, especially color-adjustable light-emitting diodes.

4. Experimental Section

Six PGC samples with the compositions (mol%) of $45SiO_2$-$15Al_2O_3$-$12Na_2O$-$28BaF_2$-$0.5ErF_3$-$1.0YbF_3$ and $45SiO_2$-$15Al_2O_3$-$12Na_2O$-$21BaF_2$-(7-x)LaF_3-xYF_3-$0.5ErF_3$-$1.0YbF_3$ (x = 0, 2, 4, 6, and 7) were prepared via the melt-quenching method. Note that Na_2O was introduced by using Na_2CO_3 for the sample preparation. For each batch, we used 10 g raw materials, each component of which has a purity of 99.99%, that were mixed and melted in an alumina crucible with a lid in the air atmosphere at 1450 °C for 45 min. Afterward, each melt was quickly cast onto a stainless-steel plate that was preheated at ≈300 °C. Each PGC sample was then annealed in a muffle furnace at 500 °C (i.e., 60 °C below T_g) for 8 h to remove thermal stress and finally slowly cooled down to room temperature. Subsequently, each sample was cut into a specific size and polished in water for use. The obtained PGC samples were named as 28BF, 0YF, 2YF, 4YF, 6YF and 7YF, respectively (**Table 2**). Additionally, the 28BF sample was heat-treated at 590 °C for 2 h and the 0YF, 2YF, 4YF, 6YF, and 7YF were heat-treated at 640 °C for 2 h to obtain HTGC samples, and then the HTGC samples were denominated as HT28BF, HT0YF, HT2YF, HT4YF, HT6YF and HT7YF, respectively (Table 2).

The T_g, T_{c1}, T_{c2} and T_c of the samples were measured using DSC (NETZSCH STA 449F3 Jupiter) by heating to 1000 °C at 10 °C min^{-1} in Ar. XRD measurements were performed to identify the crystalline phases using a PANalytical diffractometer operated at 40 KV and 40 mA with Cu-Kα (λ = 1.5406 Å) radiation. The 2θ scan range was 20°–80° with a step size of 0.013°. The bonding structure of the samples was detected using a micro-Raman spectrometer (inVia, Renishaw) with a 532 nm green HeNe laser. The morphology of the samples was characterized by field-emission SEM (QUANTA 200) using a voltage of 30 kV and transmission electron microscope (JEM-2100) equipped with energy dispersive X-ray (EDX) spectroscopy at the voltage of 200 kV.

UV–vis absorption spectra in the wavelength range from 275 to 800 nm were collected by a UV–vis spectrophotometer (Varian Cary 50). The optical transmittance per 1 mm thickness was obtained through UV–vis absorption spectra.[25] The density (ρ) of the studied samples was determined at 25 °C by Archimedes' principle, using ethanol as an immersion liquid. The UCL spectra in the wavelength range from 500 to 700 nm were recorded with a HITACHI F-7000 fluorescence spectrophotometer under the 980 nm laser excitation. The excitation power was 0.5 W and the slit was 1 nm. The absolute internal UPLQY was measured using an optical integrating sphere coupled to a fiber optic spectrometer (NQ512-1.7, 900–1700 nm, Ocean Optics). The optical response of the instrument was calibrated with a standard tungsten halogen lamp. Subsequently, the samples were put in a cuvette with an optical length of 1 mm. The absolute internal UPLQY is defined as

$$\eta_{int} = \frac{N_1}{N_2} \times 100\% \quad (2)$$

where η_{int} is the absolute internal UPLQY, N_1 is the number of emitted high-energy photons, and N_2 is the number of absorbed low-energy photons. Statistical analyses were performed through the Origin software.

Supporting Information

Supporting Information is available from the Wiley Online Library or from the author.

Acknowledgements

This work is supported by the National Natural Science Foundation of China (No. 51862020 and 12064021) and the National Natural Science Foundation of China-Yunnan Joint Fund (U2241236).

Conflict of Interest

The authors declare no conflict of interest.

Data Availability Statement

The data that support the findings of this study are available from the corresponding author upon reasonable request.

Keywords

chemical composition, cross-relaxation, crystal structure, crystallization, Up-conversion luminescence

Received: June 20, 2024
Revised: July 15, 2024
Published online: August 8, 2024

[1] P. Huang, B. Zhou, Q. Zheng, Y. Tian, M. Wang, L. Wang, J. Li, J. Wang, *Adv. Mater.* **2020**, *32*, 1905951.
[2] G. Krieke, A. Sarakovskis, *J. Eur. Ceram. Soc.* **2016**, *36*, 1715.
[3] P. P. Fedorov, A. A. Luginina, A. I. Popov, *J Fluor Chem* **2015**, *172*, 22.
[4] S. Liao, S. Jin, T. Pang, S. Lin, Y. Zheng, R. Chen, G. Xi, X. Li, B. Zhuang, F. Huang, D. Chen, *Adv. Funct. Mater.* **2024**, *34*, 2307761.
[5] B. Zhou, W. Luo, S. Liu, S. Gu, M. Lu, Y. Zhang, Y. Fan, W. Jiang, L. Wang, *Acta Mater.* **2017**, *130*, 289.
[6] X. Xu, W. Zhang, D. Yang, W. Lu, J. Qiu, S. F. Yu, *Adv. Mater.* **2016**, *28*, 8045.
[7] B. Zhou, B. Shi, D. Jin, X. Liu, *Nat. Nanotechnol.* **2015**, *10*, 924.
[8] Z. Li, D. Zhou, L. R. Jensen, J. Qiu, Y. Zhang, Y. Yue, *J. Am. Ceram. Soc.* **2021**, *104*, 4471.
[9] Z. Chen, S. Lai, H. Zhang, H. Jia, T. Wang, Q. Chen, G. Dong, C. Jiang, J. Qiu, *J. Am. Ceram. Soc.* **2017**, *100*, 612.
[10] X. Qiao, X. Fan, Z. Xue, X. Xu, Q. Luo, *J. Alloys Compd.* **2011**, *509*, 4714.
[11] M. J. Dejneka, *J Non Cryst Solids* **1998**, *239*, 149.
[12] C. Lin, C. Bocker, C. Rüssel, *Nano Lett.* **2015**, *15*, 6764.
[13] Y. Zhu, W. Xu, S. Cui, M. Liu, C. Lu, H. Song, D. H. Kim, *J. Mater. Chem. C* **2016**, *4*, 331.
[14] T. Wu, S. Zhao, R. Lei, L. Huang, S. Xu, *Mater. Res. Express* **2018**, *5*, 025201.
[15] Z. Li, J. Li, C. Chen, S. Li, J. Hu, J. F. S. Christensen, D. Zhou, L. R. Jensen, J. Ni, X. Qiao, J. Du, M. M. Smedskjaer, K. Shinozaki, Y. Zhang, J. Qiu, J. Ren, Y. Yue, *Adv. Opt. Mater.* **2024**, *12*, 2301999.
[16] Z. Li, C. Chen, W. Shen, D. Zhou, L. R. Jensen, X. Qiao, J. Ren, J. Du, Y. Zhang, J. Qiu, Y. Yue, *Adv. Opt. Mater.* **2022**, *10*, 2102713.
[17] D. Chen, Y. Zhou, Z. Wan, H. Yu, H. Lu, Z. Ji, P. Huang, *Phys. Chem. Chem. Phys.* **2015**, *17*, 7100.
[18] D. Chen, Z. Wan, Y. Zhou, P. Huang, Z. Ji, *J. Alloys Compd.* **2016**, *654*, 151.
[19] Q. Zheng, Y. Zhang, M. Montazerian, O. Gulbiten, J. C. Mauro, E. D. Zanotto, Y. Yue, *Chem. Rev.* **2019**, *119*, 7848.
[20] Z. Zhen, X. Ge, Z. Li, M. M. Smedskjaer, W. Lu, F. Yang, J. Li, Q. Hu, *Scr. Mater.* **2024**, *250*, 116179.
[21] W. Shen, Y. Yang, Z. Li, M. I. Khan, E. Cao, D. Zhou, J. Qiu, *J Non Cryst Solids* **2019**, *523*, 119579.
[22] X. Fan, J. Wang, X. Qiao, M. Wang, J. L. Adam, X. Zhang, *J. Phys. Chem. B* **2006**, *110*, 5950.
[23] F. Vetrone, V. Mahalingam, J. A. Capobianco, *Chem. Mater.* **2009**, *21*, 1847.
[24] F. Kadlec, P. Simon, N. Raimboux, *J. Phys. Chem. Solids* **1999**, *60*, 861.
[25] Z. Li, L. Tan, C. Chen, D. Zhou, L. R. Jensen, J. Ren, Y. Zhang, J. Qiu, Y. Yue, *J Non Cryst Solids* **2022**, *593*, 121773.
[26] A. Pasquarello, R. Car, *Phys. Rev. Lett.* **1998**, *80*, 5145.
[27] S. Bhattacharyya, C. Boeker, T. Heil, J. R. Jinschek, T. Höche, C. Rüssel, H. Kohl, *Nano Lett.* **2009**, *9*, 2493.
[28] J. Huang, L. Yan, Z. An, H. Wei, C. Wang, Q. Zhang, B. Zhou, *Adv. Mater.* **2024**, *36*, 2310524.
[29] Z. Li, D. Zhou, Y. Yang, P. Ren, J. Qiu, *Sci. Rep.* **2017**, *7*, 6518.
[30] X. Qiao, *Doctoral dissertation*, Zhejiang University, China **2007**.
[31] Z. Li, D. Zhou, Y. Yang, P. Ren, R. Zhu, T. Han, J. Qiu, *J. Alloys Compd.* **2018**, *731*, 1044.
[32] C. F. Bohren, D. R. Huffman, *Absorpt. Scatt. Light by Small Part*, Wiley, New Jersey, USA **2007**.
[33] H. N. RITLAND, *J. Am. Ceram. Soc.* **1955**, *38*, 86.
[34] Y. Y. Huang, A. Sarkar, P. C. Schultz, *J Non Cryst Solids* **1978**, *27*, 29.
[35] F. Huang, T. Yang, S. Wang, L. Lin, T. Hu, D. Chen, *J. Mater. Chem. C* **2018**, *6*, 12364.
[36] H. Xiao, J. Lin, R. Chen, T. Pang, P. Huang, Y. Yu, B. Zhuang, Q. Ye, R. Zhang, D. Chen, *Laser Photonics Rev.* **2024**, *18*, 2300705.
[37] J. Lin, S. Chen, W. Ye, Y. Zeng, H. Xiao, T. Pang, Y. Zheng, B. Zhuang, F. Huang, D. Chen, *Adv. Funct. Mater.* **2024**, *34*, 2314795.